

# Octupolar Weyl Superconductivity from Electron-electron Interaction

Zhiming Pan,<sup>1,2,\*</sup> Chen Lu,<sup>1,\*</sup> Fan Yang,<sup>3,†</sup> and Congjun Wu<sup>1,4,5,6,‡</sup>

<sup>1</sup>New Cornerstone Science Laboratory, Department of Physics,

School of Science, Westlake University, Hangzhou 310024, Zhejiang, China

<sup>2</sup>Department of Physics, Xiamen University, Xiamen 361005, Fujian, China

<sup>3</sup>School of Physics, Beijing Institute of Technology, Beijing 100081, China

<sup>4</sup>Institute for Theoretical Sciences, Westlake University, Hangzhou 310024, Zhejiang, China

<sup>5</sup>Key Laboratory for Quantum Materials of Zhejiang Province,

School of Science, Westlake University, Hangzhou 310024, Zhejiang, China

<sup>6</sup>Institute of Natural Sciences, Westlake Institute for Advanced Study, Hangzhou 310024, Zhejiang, China

Unconventional superconductivity arising from electron-electron interaction can manifest exotic symmetry and topological properties. We investigate the superconducting pairing symmetry problem based on the 3D cubic  $O_h$  symmetry with both weak- and strong-coupling approaches. The dominant pairing symmetries belong to the two-dimensional  $E_g$  representation at low and intermediate doping levels, and the complex mixing gap function of the  $d_{3z^2-r^2} + id_{x^2-y^2}$ -type is energetically favored in the ground state. Cooper pairs with such a symmetry do not possess orbital angular momentum (OAM) moments, which is different from other time-reversal symmetry breaking pairings such as  $p_x + ip_y$  (e.g.  $^3\text{He-A}$ ) and  $d_{x^2-y^2} + id_{xy}$  under the planar hexagonal symmetry. Instead, they develop the octupolar  $O_{xyz}$  component of OAM, which results in 8 nodal points along the body diagonal directions exhibiting an alternating distribution of monopole charges  $\pm 1$ . This leads to an intriguing 3D Weyl topological SC, which accommodates nontrivial surface states of Majorana arcs. Our results appeal for material realizations and experimental tests in optical lattices.

**Introduction** The seeking for topological superconductor (TSC) has caught enduring interests, partly due to its relation to topological quantum computation [1–3]. Much of the focus has been on fully gapped TSCs [4, 5], including the  $p$ -wave Kitaev chain [6] and two-dimensional (2D) chiral superconductors of  $(p_x + ip_y)$  and  $(d_{x^2-y^2} + id_{xy})$  symmetries [7–10]. A comprehensive classification of gapped TSCs has been developed, within the ten-fold Altland-Zirnbauer classification [11–13], which categorizes these systems based on their symmetry and dimensionality. In three dimensions (3D), there exists a particular type of TSC exhibiting point gap nodes, *i.e.*, the Weyl TSC [14], which is a superconducting analogy to the Weyl semimetal [15, 16]. The concepts of Weyl points are extended to Bogoliubov quasiparticles in superconductors [14, 17–29]. The Weyl TSCs not only inherit the non-trivial topological characteristics of Weyl semimetals but also exhibit unique superconducting properties, including gapless surface Majorana modes. Typically the Weyl semimetal or the Weyl TSC except the  $^3\text{He-A}$  phase appears in complicated compounds with spin-orbit coupling (SOC), which is a single-particle band effect from relativistic Dirac equation [30, 31].

On the other front, unconventional superconductivity (SC) from many-body interactions is of considerable interests, particularly due to its connection to the high- $T_c$  SC in cuprates [32–37]. The Hubbard model [38] is well-known as the simplest lattice model for interacting electrons only with the onsite interaction energy  $U$ , and plays an important role in the study of strong correlation physics [39, 40]. In 2D, this model exhibits the antiferromagnetic (AFM) order at half-filling in the square lattice [41–44]. Upon doping whether it could yield the

$d$ -wave SC [45–47] is still under intensive debates in numerical simulations [40].

The 3D Hubbard model has been successfully simulated in optical lattices [48], leading to the observation of the AFM order consistent with previous numerical simulations [49–53]. This success offers a new platform for studying interaction effects, allowing for precise control over the interaction strength and the temperature to explore various quantum phases [54–56]. Particularly, this opens avenues for investigating the emergence of SC in doped systems, where long-range AFM order can be suppressed, leading to the formation of superconducting phases mediated by residual short-range AFM fluctuations. It is interesting to investigate what types of exotic SCs are allowed by different 3D point groups, with a focus on the topological aspect.

In this article, we explore the pairing nature from interactions according to the cubic symmetry point group  $O_h$ . The plain Hubbard model in the 3D cubic lattice is taken as a prototype. Weak-coupling analysis is employed as well as the strong-coupling approach, consistently yielding that the doubly-degenerate  $(d_{3z^2-r^2}, d_{x^2-y^2})$ -wave pairing is dominant at low and intermediate doping levels. Ginzburg-Landau (G-L) analysis combined with numerical calculations show that the  $d + id$  complex gap function with the octupolar  $O_{xyz}$  component of orbital angular momentum (OAM) is energetically favored. This gap function exhibits 8 nodes exhibiting the alternating pattern of monopole charges  $\pm 1$  determined by the octupolar symmetries. This is a octupolar Weyl TSC hosting nontrivial surface states of topologically protected Fermi arcs. Our result does not depend on a particular model, but is general for systems with the cubic

symmetries under repulsive interactions. It opens a door for studying exotic quantum states in 3D from electron-electron interactions.

**Model and approach** The simplest repulsive Hubbard model is adopted as a prototype for illustrating the pairing symmetry problem in the 3D cubic-lattice,

$$H = -t \sum_{\langle i,j \rangle \sigma} c_{i\sigma}^\dagger c_{j\sigma} - \mu \sum_i n_i + U \sum_i n_{i\uparrow} n_{i\downarrow}, \quad (1)$$

where  $n_{i\sigma} = c_{i\sigma}^\dagger c_{i\sigma}$  represents the onsite number of fermion with spin  $\sigma$ ;  $t$  is the hopping integral;  $U$  is the on-site Hubbard repulsion;  $\langle i,j \rangle$  represents the nearest-neighbor (NN) bonds; the chemical potential  $\mu$  controls the fermion filling and the particle-hole symmetry takes place at  $\mu = U/2$ .

At half-filling, the 3D Hubbard model exhibits long-range Neel AFM order in both limits of  $U/t \rightarrow 0$  (weak coupling) and  $U/t \rightarrow +\infty$  (strong coupling) [49–52]. In the weak-coupling regime, the Fermi surface (FS) exhibits perfect nesting at the wavevector  $\mathbf{Q} = (\pi, \pi, \pi)$ , leading to the AFM order. In the strong-coupling regime, the system is Mott-insulating. The superexchange interaction is responsible for the low-energy physics as described by the AFM Heisenberg model, which shows long-range AFM ordering at low temperatures [36, 57].

Upon doping, the AFM order is gradually suppressed and completely disappear above a critical doping level. However, the short-range AFM fluctuations are still strong which could prove the pairing glue for SC. In the weak-coupling regime, a pair of fermions with opposite momenta acquire an effective attraction via exchanging spin fluctuations as well captured in the random-phase-approximation (RPA) approach [37, 58]. On other hand, in the strong-coupling regime, the exchange interaction leads to the local pairing of the resonant-valence-bond type, which upon doping develops phase coherence, leading into SC [33, 36]. Such a picture can be captured in the slave-boson-mean-field theory (SBMFT) [36, 45] treatment on the effective  $t$ - $J$  model. Details of the RPA and SBMFT approaches are provided in the Supplementary Materials (S.M.) Sec. B and C.

**Weak coupling analysis on pairing symmetry** The pairing symmetries on the cubic lattice are classified according to the IRRPs of the  $O_h$  group [59–61] see S.M. Sec. A for details. In particular, the  $d$ -wave channel on the 3D cubic lattice contains the two-fold degenerate  $E_g$  and the three-fold degenerate  $T_{2g}$  IRRPs. In contrast, on the 2D square lattice the  $d$ -wave symmetry splits to non-degenerate  $B_{1g}$  ( $d_{x^2-y^2}$ ) and  $B_{2g}$  ( $d_{xy}$ ) channels.

We first analyze the pairing symmetry in the weak coupling regime by comparing the pairing eigenvalues in each symmetry channel. The dominant channel is determined by the one with largest eigenvalue. The RPA approach is adopted to calculate pairing eigenvalues. Since the AFM ordering develops near half-filling, we avoid the extremely low doping regime (marked by the dotted lines in

Fig. 1(a, b)) in which SC is suppressed, and focus on the low and intermediate hole doping regime  $\delta \in (0.05, 0.5)$ . The numerical results of pairing eigenvalues in various symmetry channels are presented Fig. 1(a) as function of  $\delta$  for  $U/t = 1.8$ . It clearly shows that the  $E_g$  IRRP dominates in the low doping regime, i.e., the doubly-degenerate singlet pairing symmetry of ( $d_{3z^2-z^2}, d_{x^2-y^2}$ )-wave. This pairing symmetry is favored by the strong AFM fluctuations in this regime from the nearly nested FS [58, 62, 63].

The degenerate pairings belonging to a given multi-dimensional IRRP typically will be mixed below  $T_c$  due to the non-linearity of the G-L free-energy  $\mathcal{F}$ . Based on the above RPA results, we consider the gap functions  $\Delta_{1,2}$  representing the  $d_{3z^2-r^2}$  and  $d_{x^2-y^2}$  channels, respectively. Up to the quartic order,  $\mathcal{F}$  is constrained by the  $U(1) \otimes O_h$  symmetry, hence, takes the following form [61, 64],

$$\mathcal{F} = \alpha (|\Delta_1|^2 + |\Delta_2|^2) + \beta_1 (|\Delta_1|^2 + |\Delta_2|^2)^2 + \beta_2 |\Delta_1^* \Delta_2 - \Delta_2^* \Delta_1|^2, \quad (2)$$

where  $\alpha < 0$  for setting up the SC state, and  $\beta_1 > 0$  as required by the thermodynamic stability. The relative phase between  $\Delta_1$  and  $\Delta_2$  is determined by the sign of  $\beta_2$ . For  $\beta_2 < 0$ , the free-energy  $\mathcal{F}$  is minimized when  $\Delta_{1,2}$  exhibit an equal magnitude and the phase difference of  $\pm \frac{\pi}{2}$ , i.e.,

$$\Delta = (\Delta_1, \Delta_2) = \Delta(1, \pm i). \quad (3)$$

This pairing symmetry is denoted  $d_{3z^2-r^2} \pm id_{x^2-y^2}$ , abbreviated as  $d + id$  below, breaking time-reversal symmetry spontaneously. On the contrary, if  $\beta_2 > 0$ , the free-energy  $\mathcal{F}$  favors that  $(\Delta_1, \Delta_2)$  share the same phase and the ratio of their magnitudes is arbitrary. This is an example of nematic pairing symmetry denoted as  $d+d$  below. See more details of the G-L analysis in S.M. Sec.A.

The microscopic calculation of the GL parameters  $\beta_2$  would be complicated. Nevertheless, typically the weak coupling theory favors the  $d + id$  pairing. The gap function magnitude of this pairing remains the full cubic symmetry of  $O_h$  exhibiting nodal points on the FS. In contrast, the  $d + d$  pairing exhibits an anisotropic gap function with nodal lines. Hence, the distribution of  $d + id$  gap function over the FS is more uniform than that of the nematic  $d+d$  one. The free energy at the mean-field level is a convex function of the gap function, which favors its uniform distribution over the FS. Hence, the  $d + id$  pairing should be favored in the weak coupling regime, which spontaneously breaks time-reversal symmetry.

Our RPA calculations in the weak-coupling regime also yield the  $T_{2g}$  singlet pairing symmetry ( $d_{xy}, d_{xz}, d_{yz}$ ), or, the triplet  $T_{1u}$  symmetry (the  $p$ -wave) at sufficiently high doping levels  $\delta > 0.6$ . The resulting pairing ground states also realize TRSB SC [65] with exotic properties such as

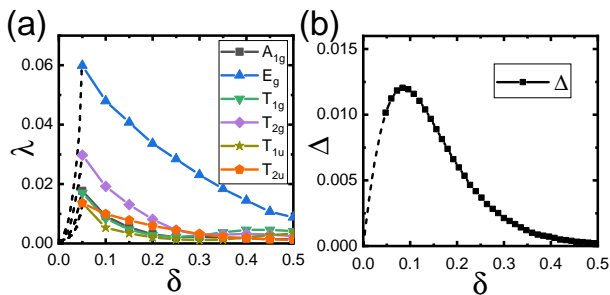


FIG. 1. The doping- $\delta$  dependence of pairing strengths. Both the weak coupling RPA and strong coupling SBMFT methods show the dominance of the  $E_g$  symmetry pairing. Pairing quickly develops as doping is introduced, and gradually decrease as doping goes large. (a). RPA analysis on the pairing eigenvalues  $\lambda$  versus  $\delta$  for different pairing symmetries.  $U/t = 1.8$  is adopted. (b). The SBMFT calculation of  $\Delta$  versus  $\delta$  for the  $t$ - $J$  model.  $J/t = 0.4$  ( $U/t = 10$ ) is adopted.

node points and the sextetting order (charge 6e) [66–70]. These results are provided in the S.M. Sec. B.

**Strong coupling analysis on pairing symmetry** We next turn to the strong coupling regime, in which the low energy physics is described by the effective  $t$ - $J$  model,

$$H = -t \sum_{\langle i,j \rangle \sigma} c_{i\sigma}^\dagger c_{j\sigma} + J \sum_{\langle i,j \rangle} (\mathbf{S}_i \cdot \mathbf{S}_j - \frac{1}{4}), \quad (4)$$

where  $\mathbf{S}_i$  is the spin operator at site  $i$  and  $J = 4t^2/U$ . Note that the no-double-occupant constraint is imposed on the Hilbert space. The superexchange interaction  $J$  induces the NN pairings  $\Delta_{x,y,z}$  along the  $x, y$  and  $z$ -directions, respectively. Calculations based on SBMFT reveal that the NN pairings take the form of  $(\Delta_x, \Delta_y, \Delta_z) = \Delta(1, e^{i2\pi/3}, e^{i4\pi/3})$  or its symmetry equivalences. This is the same as the  $d + id$  symmetry consistent with the RPA results in the weak-coupling regime. The doping  $\delta$ -dependence of the gap function strength  $\Delta$  is depicted in Fig. 1(b), which shows that as increasing doping SC quickly emerges and then gradually decreases, exhibiting a dome feature similar to  $\lambda$ 's dependence on  $\delta$  as shown in Fig. 1(a).

**Octupolar and Weyl TSC** The  $d + id$  pairing with the  $E_g$  bases is quite different from the  $p_x + ip_y$  type of  $^3\text{He-A}$  [71, 72], and is also different from the  $d_{x^2-y^2} + id_{xy}$  type in hexagonal lattices [8–10, 61]. The pairing symmetries of the latter two cases carry the orbital angular momentum (OAM) quantum number with  $L_z = 1$  and 2, respectively. In contrast,  $d_{x^2-y^2}$  and  $d_{xy}$  cannot be connected by  $L_\pm = L_x \pm iL_y$ . The expectation values of  $L_{x,y,z}$  and its quadrupole tensor components vanish in the  $d + id$  state of the  $E_g$  version. Viewed from the body diagonal directions, the system exhibits the alternating vorticities of  $\pm 2$ , *i.e.*, the octupolar pattern, as illustrated in Fig. 2 (a) and (b). Indeed, a Cooper pair with such a symmetry exhibits a non-zero OAM octupole component

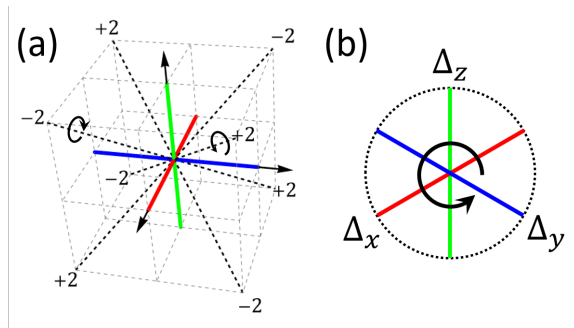


FIG. 2. Illustration of the NN pairing configuration with the phases of 1,  $e^{i2\pi/3}$ ,  $e^{i4\pi/3}$  marked as  $R, G, B$ , respectively. (a) The vorticity projection along body diagonal lines exhibits the alternating pattern of  $\pm 2$ . (b) The  $[111]$ -direction shows the vorticity of 2. A Cooper pair with such a symmetry carries a non-zero OAM octupolar component  $O_{xyz}$ . Consequently, the corresponding gap function exhibits 8 nodes on the FS.

defined as  $O_{xyz} = \frac{1}{3!} \sum_P L_i L_j L_k$  with  $P$  representing the permutations of  $x, y, z$ .

The octupolar pairing symmetry of  $d_{3z^2-r^2} \pm id_{x^2-y^2}$  obtained at the low and intermediate doping regimes exhibits interesting symmetry and topological properties. Without loss of generality, its gap function in momentum space is expressed as

$$\Delta(\mathbf{k}) = \Delta (\cos k_x + e^{i\frac{2\pi}{3}} \cos k_y + e^{i\frac{4\pi}{3}} \cos k_z). \quad (5)$$

Its nodal direction appear along the body diagonal ones  $(\pm 1, \pm 1, \pm 1)$  in consistent with the octupolar symmetry. In comparison, the  $p_x + ip_y$  pairing can be viewed as the dipolar symmetry exhibiting nonzero  $L_z$  and the nodal lines along the  $z$ -axis. In the Nambu representation, the Bogoliubov-de Gennes Hamilton is given by,

$$H_{\text{BdG}} = \sum_{\mathbf{k}} \begin{pmatrix} c_{\mathbf{k}\uparrow}^\dagger & c_{-\mathbf{k}\downarrow} \end{pmatrix} H(\mathbf{k}) \begin{pmatrix} c_{\mathbf{k}\uparrow} \\ c_{-\mathbf{k}\downarrow}^\dagger \end{pmatrix}, \quad (6)$$

$$H(\mathbf{k}) = \varepsilon(\mathbf{k})\tau_3 + \text{Re}\Delta(\mathbf{k})\tau_1 - \text{Im}\Delta(\mathbf{k})\tau_2,$$

where  $\varepsilon(\mathbf{k}) = -2t(\cos k_x + \cos k_y + \cos k_z) - \mu$  is the kinetic energy and  $\tau_i$  is the Pauli matrix in the Nambu space. The quasi-particle dispersion exhibits 8 nodal points located at the intersections of the body diagonal directions and the FS, *i.e.*,  $\mathbf{k}_{\text{node}} = \frac{k_F}{\sqrt{3}}(\pm 1, \pm 1, \pm 1)$ , where  $k_F$  is the Fermi wavevector. Due to TRSB, these node points could be considered as ‘‘Weyl nodes’’ for the Bogoliubov quasiparticles [14, 16].

Near the nodal points, the quasi-particles exhibit the following the linear dispersion relation,

$$H(\mathbf{p}) = (\mathbf{v}_1 \cdot \mathbf{p})\tau_1 + (\mathbf{v}_2 \cdot \mathbf{p})\tau_2 + (\mathbf{v}_3 \cdot \mathbf{p})\tau_3 \quad (7)$$

where  $\mathbf{p} \equiv \mathbf{k} - \mathbf{k}_{\text{node}}$  is the relative momentum with respect to  $\mathbf{k}_{\text{node}}$  and  $\mathbf{v}_i$  ( $i = 1, 2, 3$ ) are unit vectors pointing along the local velocity orientations, see S.M. Sec.D

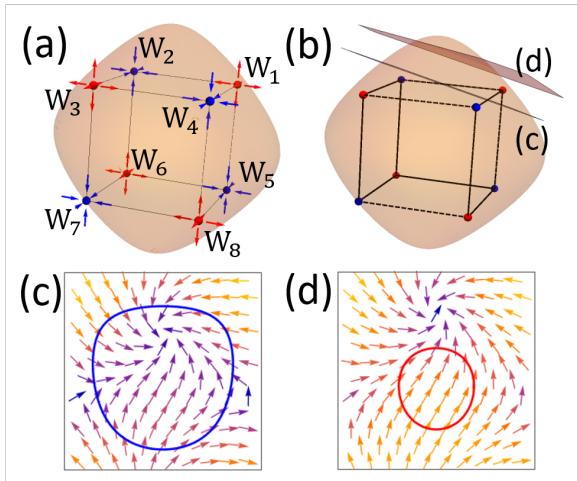


FIG. 3. (a). The 8 Weyl points around the FS with alternating monopole charges exhibiting the octupolar pattern. The red (blue) circles indicate Weyl points acting as positive (negative) magnetic monopoles. (b). Cross-sections with topologically non-trivial and trivial 2D pairing configurations, shown in (c) with  $C = 1$  and (d) with  $C = 0$ , respectively. Small arrows indicate the orientations of the pairing phase.

for details. The 3D chirality (monopole charge) associated with a given Weyl node can be directly calculated as  $C = \text{Sgn}[\mathbf{v}_1 \cdot (\mathbf{v}_2 \times \mathbf{v}_3)] = \pm 1$  [15, 22]. The Weyl node at  $\mathbf{k}_{\text{node}}$  with  $C = +1(-1)$  acts as a positive (negative) magnetic monopole in momentum space, and its chirality is determined by the octupolar vorticity along  $\mathbf{k}_{\text{node}}$ . Consequently, the monopole charges of the 8 Weyl nodes are marked in Fig. 3(a), exhibiting the octupolar pattern. This low-energy effective theory suggests a Weyl superconductor [14], which is a superconducting counterpart to the Weyl semimetal.

The emergence of Bogoliubov-Weyl points in this pairing state is protected by topological reasons. Construct an arbitrary 2D cross-section that intersects the 3D FS while avoiding the Weyl points. It results in a 2D gapped superconductor, which can be topologically either trivial or non-trivial depending on the location of the cross-section. As illustrated in Fig. 3(b), as the section plane is shifted to cross a Weyl point, the 2D Chern number describing the pairing phase winding around the 2D FS [4, 5] changes from  $C = 1$  before crossing the point (c) to  $C = 0$  afterward (d). In other words, the 2D SC within the slice evolves from a topological one to a trivial one. Hence, an intermediate Weyl node is unavoidable.

With the bulk-boundary correspondence, the Weyl SC exhibits non-trivial Fermi-arc surface states, which are the Majorana arcs of the Bogoliubov quasi-particles. Specifically, we consider the (110) surface shown in Fig. 4(a). The projection of the 8 Weyl nodes  $W_i$  ( $i = 1 \sim 8$ ) onto this surface results in 8 points  $\tilde{W}_i$  marked in the surface Brillouin Zone (BZ) shown in Fig. 4(b). To conveniently visualize the special role of the Weyl points

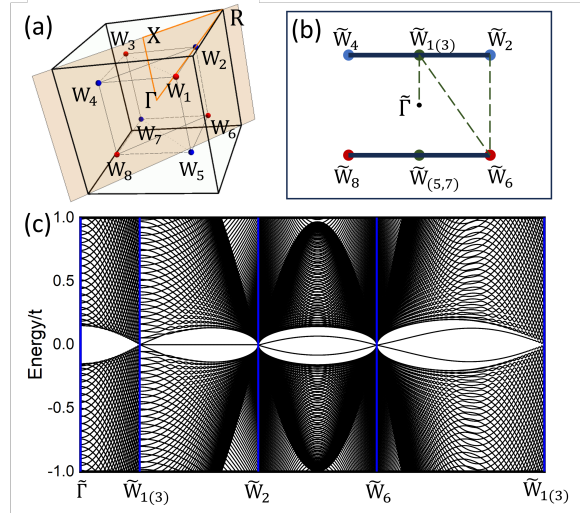


FIG. 4. (a). Schematic diagram for the (110)-surface (shadow plane). (b). Projected Weyl nodes  $\tilde{W}_i$  in the (110) surface BZ and the Fermi arcs (solid lines). (c). Energy spectrum along the path  $\tilde{\Gamma} - \tilde{W}_{1(3)} - \tilde{W}_2 - \tilde{W}_6 - \tilde{W}_{1(3)}$  marked in (b) (dashed lines) for  $|\Delta| = 0.1t$  and  $\mu = -3t$ .

in generating gapless surface modes, we calculate the surface spectrum along the path  $\tilde{\Gamma} - \tilde{W}_{1(3)} - \tilde{W}_2 - \tilde{W}_6 - \tilde{W}_{1(3)}$  in the surface BZ (the dashed lines in Fig. 4(b)) as shown in Fig. 4(c). Particularly, along the path from  $\tilde{W}_{1(3)}$  to  $\tilde{W}_2$ , there exist a line of gapless modes forming the Fermi arc  $\tilde{W}_{1(3)} - \tilde{W}_2$  exhibited in Fig. 4(b). The other Fermi arcs in Fig. 4(b) are obtained by symmetry. Note that the Fermi arcs  $\tilde{W}_{1(3)} - \tilde{W}_2$  and  $\tilde{W}_{1(3)} - \tilde{W}_4$  are connected at the  $\tilde{W}_{1(3)}$  point on the (110) surface.

**Conclusion and Discussion** The SC state arising from electron-electron interactions within the context of 3D cubic symmetry is investigated, using the Hubbard model on a 3D cubic lattice as a prototype. The results from RPA calculations in the weak coupling regime supplemented by G-L analysis, as well as strong-coupling calculations, reveal the emergence of a TRSB  $d + id$  pairing upon doping. This state suggests a novel octupolar Weyl TSC, with topological protected Bogoliubov-Weyl nodes and surface Majorana arcs.

The exotic Weyl SC might be realized in certain materials with cubic symmetry or related structure. Previous studies have suggested that heavy fermion compounds with cubic symmetry, such as  $\text{UBe}_{13}$  and  $\text{CeIn}_3$ , could exhibit unconventional SC [73, 74]. Recently, experimental signature of  $d$ -wave pairing has been proposed in  $\text{LiTi}_2\text{O}_4$  [75]. Similar  $d + id$  state has been suggested for high- $T$  phase cubic  $\text{CsW}_2\text{O}_6$  [76]. Recent advancements in simulating the AFM phase transition in the 3D Hubbard model [48] provide a promising pathway for realizing the exotic Weyl SC state proposed in this study upon doping.

Notably, in contrast to 2D systems, which are signif-

icantly affected by stronger quantum fluctuations, the AFM order in 3D is more robust [77]. Upon doping, the 3D AFM order will persist over a broader doping range than in its 2D counterpart. To facilitate the observation of SC, it is crucial to include factors that can suppress the AFM order, such as frustration introduced by next-NN hopping or structural modifications to the lattice. These factors can be effectively manipulated in optical lattice systems, offering potential experimental avenues for realizing the predicted Weyl SC state.

*Acknowledgments* We are grateful to Sheng-Shan Qin, Cheng-Cheng Liu and Yan-Xia Xing for stimulating discussions. C. W. and F. Y. are supported by the National Natural Science Foundation of China (NSFC) under the Grant No. 12234016, and also supported by the NSFC under the Grant Nos. 12174317 and 12074031, respectively. C.L. is supported by the National Natural Science Foundation of China under the Grants No. 12304180. This work has been supported by the New Cornerstone Science Foundation.

---

\* These two authors contributed equally to this work.

† [yangfan\\_blg@bit.edu.cn](mailto:yangfan_blg@bit.edu.cn)

‡ [wucongjun@westlake.edu.cn](mailto:wucongjun@westlake.edu.cn)

- [1] A. Y. Kitaev, *Annals of physics* **303**, 2 (2003).
- [2] C. Nayak *et al.*, *Reviews of Modern Physics* **80**, 1083 (2008).
- [3] S. D. Sarma, M. Freedman, and C. Nayak, *npj Quantum Information* **1**, 1 (2015).
- [4] M. Z. Hasan and C. L. Kane, *Reviews of modern physics* **82**, 3045 (2010).
- [5] X.-L. Qi and S.-C. Zhang, *Reviews of modern physics* **83**, 1057 (2011).
- [6] A. Y. Kitaev, *Physics-uspekhi* **44**, 131 (2001).
- [7] A. P. Mackenzie and Y. Maeno, *Reviews of Modern Physics* **75**, 657 (2003).
- [8] C. Honerkamp, *Physical Review B* **68**, 104510 (2003).
- [9] M. Ogata, *Journal of the Physical Society of Japan* **72**, 1839 (2003).
- [10] R. Nandkishore, L. S. Levitov, and A. V. Chubukov, *Nature Physics* **8**, 158 (2012).
- [11] A. Altland and M. R. Zirnbauer, *Physical Review B* **55**, 1142 (1997).
- [12] A. Kitaev, in *AIP conference proceedings*, American Institute of Physics (PUBLISHER, ADDRESS, 2009), No. 1, pp. 22–30.
- [13] S. Ryu, A. P. Schnyder, A. Furusaki, and A. W. Ludwig, *New Journal of Physics* **12**, 065010 (2010).
- [14] Y. Li and C. Wu, *Scientific reports* **2**, 392 (2012).
- [15] X. Wan, A. M. Turner, A. Vishwanath, and S. Y. Savrasov, *Phys. Rev. B* **83**, 205101 (2011).
- [16] N. Armitage, E. Mele, and A. Vishwanath, *Reviews of Modern Physics* **90**, 015001 (2018).
- [17] T. Meng and L. Balents, *Physical Review B* **86**, 054504 (2012).
- [18] J. D. Sau and S. Tewari, *Physical Review B—Condensed Matter and Materials Physics* **86**, 104509 (2012).
- [19] S. A. Yang, H. Pan, and F. Zhang, *Physical review letters* **113**, 046401 (2014).
- [20] M. H. Fischer *et al.*, *Physical Review B* **89**, 020509 (2014).
- [21] G. Bednik, A. Zyuzin, and A. Burkov, *Physical Review B* **92**, 035153 (2015).
- [22] G. E. Volovik, *JETP letters* **105**, 273 (2017).
- [23] N. F. Yuan, W.-Y. He, and K. T. Law, *Physical Review B* **95**, 201109 (2017).
- [24] R. Okugawa and T. Yokoyama, *Physical Review B* **97**, 060504 (2018).
- [25] Y. Li and F. Haldane, *Physical review letters* **120**, 067003 (2018).
- [26] S. Sumita and Y. Yanase, *Physical Review B* **97**, 134512 (2018).
- [27] I. M. Hayes *et al.*, arXiv preprint arXiv:2002.02539 (2020).
- [28] R. Nakai and K. Nomura, *Physical Review B* **101**, 094510 (2020).
- [29] M. Hori, R. Okugawa, K. Tanaka, and T. Tohyama, *Phys. Rev. Res.* **6**, 033088 (2024).
- [30] A. Manchon *et al.*, *Nature materials* **14**, 871 (2015).
- [31] M. Sato and Y. Ando, *Reports on Progress in Physics* **80**, 076501 (2017).
- [32] J. G. Bednorz and K. A. Müller, *Zeitschrift für Physik B Condensed Matter* **64**, 189 (1986).
- [33] P. W. Anderson, *science* **235**, 1196 (1987).
- [34] V. J. Emery, *Phys. Rev. Lett.* **58**, 2794 (1987).
- [35] E. Dagotto, *Reviews of Modern Physics* **66**, 763 (1994).
- [36] P. A. Lee, N. Nagaosa, and X.-G. Wen, *Reviews of modern physics* **78**, 17 (2006).
- [37] D. J. Scalapino, *Rev. Mod. Phys.* **84**, 1383 (2012).
- [38] J. Hubbard, *Proceedings of the Royal Society of London. Series A. Mathematical and Physical Sciences* **276**, 238 (1963).
- [39] D. P. Arovas, E. Berg, S. A. Kivelson, and S. Raghu, *Annual review of condensed matter physics* **13**, 239 (2022).
- [40] M. Qin *et al.*, *Annual Review of Condensed Matter Physics* **13**, 275 (2022).
- [41] J. E. Hirsch, *Physical Review B* **31**, 4403 (1985).
- [42] J. Hirsch and S. Tang, *Physical review letters* **62**, 591 (1989).
- [43] M. Imada, A. Fujimori, and Y. Tokura, *Reviews of modern physics* **70**, 1039 (1998).
- [44] C. Varney *et al.*, *Physical Review B—Condensed Matter and Materials Physics* **80**, 075116 (2009).
- [45] G. Kotliar and J. Liu, *Physical Review B* **38**, 5142 (1988).
- [46] P. Monthoux, A. Balatsky, and D. Pines, *Physical review letters* **67**, 3448 (1991).
- [47] D. J. Scalapino, *Physics Reports* **250**, 329 (1995).
- [48] H.-J. Shao *et al.*, *Nature* **632**, 267–272 (2024).
- [49] J. E. Hirsch, *Phys. Rev. B* **35**, 1851 (1987).
- [50] R. Scalettar, D. Scalapino, R. Sugar, and D. Toussaint, *Physical Review B* **39**, 4711 (1989).
- [51] P. Kent, M. Jarrell, T. Maier, and T. Pruschke, *Physical Review B—Condensed Matter and Materials Physics* **72**, 060411 (2005).
- [52] G. Rohringer, A. Toschi, A. Katanin, and K. Held, *Physical review letters* **107**, 256402 (2011).
- [53] R. A. Hart *et al.*, *Nature* **519**, 211 (2015).
- [54] D. Jaksch and P. Zoller, *Annals of physics* **315**, 52 (2005).
- [55] T. Esslinger, *Annu. Rev. Condens. Matter Phys.* **1**, 129 (2010).
- [56] A. Bohrdt *et al.*, *Annals of Physics* **435**, 168651 (2021).
- [57] P. W. Anderson, *Physical Review* **115**, 2 (1959).

- [58] D. Scalapino, E. Loh Jr, and J. Hirsch, *Physical Review B* **34**, 8190 (1986).
- [59] G. Volovik and L. Gor'kov, *JETP lett* **39**, 550 (1984).
- [60] G. Volovik and L. P. Gor'kov, *JETP* **61**, 843 (1985).
- [61] M. Sigrist and K. Ueda, *Reviews of Modern physics* **63**, 239 (1991).
- [62] S. Raghu, S. Kivelson, and D. Scalapino, *Physical Review B* **81**, 224505 (2010).
- [63] J. Ehrlich and C. Honerkamp, *Physical Review B* **102**, 195108 (2020).
- [64] D. Agterberg, V. Barzykin, and L. P. Gor'kov, *Physical Review B* **60**, 14868 (1999).
- [65] C. Xu, W. Yang, and C. Wu, *Physical Review B* **108**, 094509 (2023).
- [66] D. Agterberg, M. Geracie, and H. Tsunetsugu, *Physical Review B—Condensed Matter and Materials Physics* **84**, 014513 (2011).
- [67] S. Zhou and Z. Wang, *Nature Communications* **13**, 7288 (2022).
- [68] Z. Pan, C. Lu, F. Yang, and C. Wu, *Science China Physics, Mechanics & Astronomy* **67**, 287412 (2024).
- [69] L.-F. Zhang, Z. Wang, and X. Hu, *Communications Physics* **7**, 210 (2024).
- [70] J. Ge *et al.*, *Physical Review X* **14**, 021025 (2024).
- [71] A. J. Leggett, *Reviews of Modern Physics* **47**, 331 (1975).
- [72] G. E. Volovik, *The universe in a helium droplet* (OUP Oxford, ADDRESS, 2003), Vol. 117.
- [73] Y. Yanase *et al.*, *Physics Reports* **387**, 1 (2003).
- [74] C. Pfeleiderer, *Reviews of Modern Physics* **81**, 1551 (2009).
- [75] H. Xue *et al.*, *ACS nano* **16**, 19464 (2022).
- [76] S. V. Streltsov, I. I. Mazin, R. Heid, and K.-P. Bohnen, *Physical Review B* **94**, 241101 (2016).
- [77] R. Arita, K. Kuroki, and H. Aoki, *Physical Review B* **60**, 14585 (1999).

## SUPPLEMENTAL MATERIAL

### A. Pairing symmetries and Ginzburg-Landau analysis

The pairing symmetries on the cubic lattice are classified according to the irreducible representations (IRRPs) of the  $O_h$  group in Tab. A1 [59–61], which can be intuitively represented by the lowest order symmetry polynomials. The lower index  $g$  corresponds to even parity spin singlet pairing symmetries (e.g.  $s$  and  $d$ -waves), and  $u$  represents odd parity spin triplet pairing symmetries (e.g.  $p$ - and  $f$ - waves).

For the two-fold degenerate superconductivity (SC) within the  $E_g$  IRRP, the Ginzburg-Landau free energy takes the following form [61]

$$\mathcal{F} = \alpha(|\Delta_1|^2 + |\Delta_2|^2) + \beta_1(|\Delta_1|^2 + |\Delta_2|^2)^2 + \beta_2|\Delta_1^*\Delta_2 - \Delta_2^*\Delta_1|^2, \quad (\text{A1})$$

For  $\beta_2 < 0$ , the phase difference between the two components is  $\pm\frac{\pi}{2}$ , leading to a  $1 : \pm i$  mixing of the pairing functions. This state exhibits spontaneously time-reversal symmetry breaking (TRSB), resulting in Weyl SC. Conversely, when  $\beta_2 > 0$ , the two components share the same phase, resulting in an order parameter of the form:

$$\vec{\Delta} = (\Delta_1, \Delta_2) \propto (\cos\theta, \sin\theta) \quad (\text{A2})$$

which corresponds to a nematic state that reduces the full rotational symmetry of the  $O_h$  group to its subgroup. This quartic-order Ginzburg-Landau theory exhibits an accidental continuous degeneracy for the nematic state, which can be lifted through the inclusion of higher-order terms. To resolve this degeneracy, a sixth-order term respecting the  $O_h$  symmetry in the free energy can be added [61]:

$$\mathcal{F}_\gamma = \gamma_1(|\Delta_1|^2 + |\Delta_2|^2)^3 + \gamma_2(|\Delta_1|^2 + |\Delta_2|^2)|\Delta_1^2 + \Delta_2^2|^2 + \gamma_3|\Delta_1|^2|3\Delta_2^2 - \Delta_1^2|^2. \quad (\text{A3})$$

It is evident that a positive  $\gamma_3$  favors the nematic state  $(\Delta_1, \Delta_2) \propto (0, 1)$ , while a negative  $\gamma_3$  supports the state  $(\Delta_1, \Delta_2) \propto (1, 0)$ .

Additionally, the  $O_h$  symmetry permits the existence of three-fold degenerate SC state, belonging to the  $T_{1g}$ ,  $T_{2g}$ ,  $T_{1u}$  or  $T_{2u}$  IRRP, as detailed in Tab. A1. They are characterized by three-component order parameters  $\Delta_a$  ( $a = 1, 2, 3$ ). Up to quartic order, the Ginzburg-Landau free energy for these states is expressed as follows [61],

$$\mathcal{F} = \alpha \sum_a |\Delta_a|^2 + \beta_1 \left( \sum_a |\Delta_a|^2 \right)^2 + \beta_2 \left| \sum_a \Delta_a^2 \right|^2 + \beta_3 \left( |\Delta_1|^2 |\Delta_2|^2 + |\Delta_2|^2 |\Delta_3|^2 + |\Delta_3|^2 |\Delta_1|^2 \right), \quad (\text{A4})$$

where we require  $\alpha < 0$  and  $\beta_1 > 0$  in the SC state. The sign of  $\beta_2$  is crucial in determining the configuration of the SC state: a positive  $\beta_2 > 0$  favors a complex mixing structure among the components, where a negative  $\beta_2 < 0$  favors a real mixing.

The possible ground states and their associated free energies are summarized in Tab. A2. The ground state is attained when the free energy is minimized [61]. Notably, a nematic state featuring only two non-zero components is not favored within the relevant parameter regime. For the case where  $\beta_3 < 0 < \beta_2$ , a TRSB state emerges as the preferred configuration, with the order parameter taking the complex structure  $(\Delta_1, \Delta_2, \Delta_3) \propto (1, e^{\pm i2\pi/3}, e^{\pm i4\pi/3})$ .

(even) Rep.	Basis functions	
$A_{1g}$	1	$s$ -wave
	$x^2 + y^2 + z^2$	$s$ -wave
$A_{2g}$	$(x^2 - y^2)(y^2 - z^2)(z^2 - x^2)$	
$E_g$	$\{3z^2 - r^2, x^2 - y^2\}$	$d$ -wave
$T_{1g}$	$\{xy(x^2 - y^2), \dots\}$	$g$ -wave
$T_{2g}$	$\{xy, yz, zx\}$	$d$ -wave
(odd) Rep.	Function	
$A_{2u}$	$xyz$	$f$ -wave
$T_{1u}$	$\{x, y, z\}$	$p$ -wave
$T_{2u}$	$\{x(y^2 - z^2), \dots\}$	$f$ -wave

TABLE A1. IRRPs of gap functions for the octahedral group  $O_h$ , including both the singlet even parity and triplet odd parity channels.

$(\Delta_1, \Delta_2, \Delta_3)$	Free energy	condition
$e^{i\theta}(1, 0, 0)$	$-4\alpha/(\beta_1 + \beta_2)$	$\beta_3 > 0, 4\beta_2 < \beta_3$
$e^{i\theta}(1, 1, 0)$	$-4\alpha/(\beta_1 + \beta_2 + \beta_3/4)$	#
$e^{i\theta}(1, i, 0)$	$-4\alpha/(\beta_1 + \beta_3/4)$	$0 < \beta_3 < 4\beta_2$
$e^{i\theta}(1, 1, 1)$	$-4\alpha/(\beta_1 + \beta_2 + \beta_3/3)$	$\beta_2, \beta_3 < 0$
$e^{i\theta}(1, \omega, \omega^2)$	$-4\alpha/(\beta_1 + \beta_3/3)$	$\beta_3 < 0 < \beta_2$

TABLE A2. Possible ground states configuration  $(\Delta_1, \Delta_2, \Delta_3)$  and associated free energy. The conditions for each state are provided in the last column.

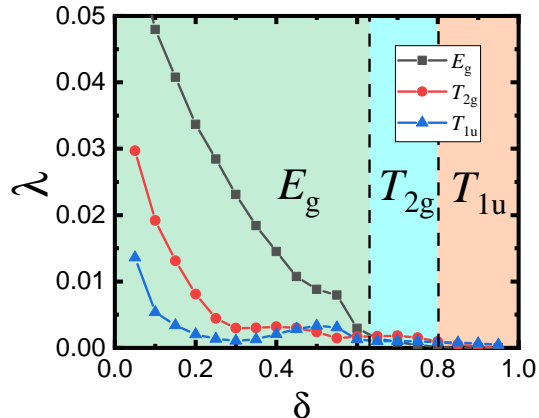


FIG. A1. Dominated pairing strength eigenvalues  $\lambda$  and the phase diagram under doping  $\delta$  for  $U/t = 1.8$ . Near half-filling (lower  $\delta$ ), the SC state is dominated by  $d$ -wave  $E_g$  representation. As the doping level increases, the SC state evolves into the  $d$ -wave  $T_{2g}$  representation. At higher doping, the SC state is controlled by a  $p$ -wave triplet pairing belonging to  $T_{1u}$  representation.

### B. Numerical simulation in the weak-coupling regime and the pairing natures

The associated phase diagram for different doping levels  $\delta$  based on random-phase approximation (RPA) in the weak-coupling regime is summarized in Fig. A1. Near half-filling, a two-fold IRRP within  $d$ -wave pairing ( $d_{3z^2-r^2}, d_{x^2-y^2}$ ) is favored. As the doping  $\delta$  increases, the  $d$ -wave pairing symmetry transitions from a two-fold degenerate  $E_g$  IRRP to a three-fold degenerate  $T_{2g}$  IRRP ( $d_{xy}, d_{yz}, d_{zx}$ ) at intermediate doping levels. At high doping levels, particularly near  $\delta = 1$  with low electron densities, the system exhibits a  $p$ -wave triplet pairing corresponding to the  $T_{1u}$  IRRP.

At intermediate doping levels, a TRSB superconducting state within the  $T_{2g}$  representation may emerge. This state corresponds to the following form of the order parameter:

$$\Delta(\mathbf{k}) = \frac{\Delta_0}{\sqrt{3}}(k_x k_y + e^{i\frac{2\pi}{3}} k_y k_z + e^{i\frac{4\pi}{3}} k_z k_x), \quad (\text{A5})$$

which exhibits an eight-fold degeneracy linked by the mirror symmetry or time-reversal transformation. In this state, the full  $O_h$  point group symmetry is reduced to its subgroup. The quasi-particle dispersion for this TRSB  $T_{2g}$  state features a total of  $6 + 2$  nodal points, denoted as  $\mathbf{k}_{\text{node}}$ ,

$$\mathbf{k}_{\text{node}} = k_F(\pm 1, 0, 0), \quad k_F(0, \pm 1, 0), \quad k_F(0, 0, \pm 1), \quad \pm k_F(1, 1, 1).$$

For the TRSB superconducting state in the spin-triplet  $T_{1u}$  representation, the  $d$ -vector is expressed by:

$$d(\mathbf{k}) \propto \hat{\mathbf{x}}(\omega^2 k_y - \omega k_z) + \hat{\mathbf{y}}(k_z - \omega^2 k_x) + \hat{\mathbf{z}}(\omega k_x - k_y). \quad (\text{A6})$$

with  $\omega = e^{i2\pi/3}$ . This TRSB state is non-unitary, exhibiting net spin polarization due to finite  $\mathbf{q} = i\mathbf{d} \times \mathbf{d}^*$ . Moreover, it also exhibits nodal points.

Additionally, the three-fold degenerate SC represented by the three components pairing gaps  $(\Delta_1, \Delta_2, \Delta_3)$  may realize a sextetting order, where six electrons combine to form a bound state, commonly referred to as charge-6e order. Intriguingly, the  $p$ -wave triplet representation  $T_{1u}$  might realize a sextetting pairing with distinct angular momentum characteristics, differing from the singlet sextetting pairing within the  $T_{2g}$  representation.



### C. Strong coupling $t$ - $J$ model and SBMFT

In the strong coupling limit, the low-energy effective theory is described by a  $t$ - $J$  model under the no-double occupancy constraint,

$$H_{tJ} = -t \sum_{\langle i,j \rangle \sigma} \mathcal{P}(c_{i\sigma}^\dagger c_{j\sigma} + \text{h.c.}) \mathcal{P} + J \sum_{\langle i,j \rangle} \left( \mathbf{S}_i \cdot \mathbf{S}_j - \frac{1}{4} \right), \quad (\text{A7})$$

where  $\mathbf{S}_i = \frac{1}{2} c_i^\dagger \boldsymbol{\sigma} c_i$  is the spin operator at lattice site  $i$  and  $J = 4t^2/U$  is the nearest-neighbor (NN) antiferromagnetic (AFM) spin superexchange in the large- $U$  limit. The operator  $\mathcal{P}$  projects out double-occupied states, reflecting strong correlation effects.

The constrained  $t$ - $J$  model can be analyzed using slave-boson mean-field theory (SBMFT) [36, 45]. In this framework, the bare electron operators are expressed in terms of auxiliary holon and spinon operators, maintaining the no-double occupancy constraint:

$$c_{i\sigma}^\dagger \rightarrow f_{i\sigma}^\dagger h_i, \quad c_{i\sigma} \rightarrow h_i^\dagger f_{i\sigma}, \quad \sum_{\sigma} f_{i\sigma}^\dagger f_{i\sigma} + h_i^\dagger h_i = 1, \quad (\text{A8})$$

where  $h_i^\dagger$  and  $f_{i\sigma}^\dagger$  are the holon and spinon creation operators at the lattice site  $i$ , respectively. In the ground state, the holon condenses, allowing us to replace the holon operator with its condensation density  $h_i = h_j^\dagger = \sqrt{\delta}$ .

Within the mean-field theory, the following spinon hopping and pairing order parameters are introduced,

$$\chi_{ij} = \langle f_{j\uparrow}^\dagger f_{i\uparrow} + f_{j\downarrow} f_{i\downarrow} \rangle \equiv \chi_{j-i}, \quad \tilde{\Delta}_{ij} = \langle f_{j\downarrow} f_{i\uparrow} - f_{j\uparrow} f_{i\downarrow} \rangle \equiv \tilde{\Delta}_{j-i}, \quad (\text{A9})$$

assuming translational symmetry, such that the order parameters depend only on the relative distance between sites. We focus on the NN hoppings and pairings along the three directions  $\mu = x, y, z$ , i.e.,  $\chi_\mu = \chi_{i, i+\hat{\mu}}$  and  $\tilde{\Delta}_\mu = \tilde{\Delta}_{i, i+\hat{\mu}}$ . The spin-exchange can be decomposed as follows:

$$J \mathbf{S}_i \cdot \mathbf{S}_j = -\frac{3}{8} J \left[ \chi_{ij} (f_{i\uparrow}^\dagger f_{j\uparrow} + f_{i\downarrow}^\dagger f_{j\downarrow}) + \text{h.c.} \right] - \frac{3}{8} J \left[ \tilde{\Delta}_{ij} (f_{i\uparrow}^\dagger f_{j\downarrow}^\dagger - f_{i\downarrow}^\dagger f_{j\uparrow}^\dagger) + \text{h.c.} \right] + \text{const.} \quad (\text{A10})$$

The slave-boson mean-field Hamiltonian for the spinon field in momentum space is expressed as:

$$H_f = \sum_{\mathbf{k}\sigma} \varepsilon(\mathbf{k}) f_{\mathbf{k}\sigma}^\dagger f_{\mathbf{k}\sigma} + \sum_{\mathbf{k}} \left[ \tilde{\Delta}(\mathbf{k}) (f_{\mathbf{k}\uparrow}^\dagger f_{-\mathbf{k}\downarrow}^\dagger - f_{\mathbf{k}\downarrow}^\dagger f_{-\mathbf{k}\uparrow}^\dagger) + \text{h.c.} \right] \quad (\text{A11})$$

where the kinetic energy and spinon pairing field are given by

$$\varepsilon(\mathbf{k}) = -2 \left( t\delta + \frac{3}{8} J\chi \right) \sum_{\mu} \cos(k_\mu) - \mu, \quad \tilde{\Delta}(\mathbf{k}) = -\frac{3}{8} J \sum_{\mu} \tilde{\Delta}_\mu \cos(k_\mu).$$

Here, we assume a symmetric hopping fields with  $\chi_x = \chi_y = \chi_z \equiv \chi$ . The physical superconducting order parameter is represented as  $\Delta \propto \delta \tilde{\Delta}$ , where  $\delta$  is the holon condensation density.

The pairing configuration  $(\Delta_x, \Delta_y, \Delta_z) \propto (1, 1, 1)$  corresponds to a  $s$ -wave pairing. In contrast, the pairing configuration  $(\Delta_x, \Delta_y, \Delta_z) \propto (1, -1, 0)$  and  $(\Delta_x, \Delta_y, \Delta_z) \propto (-1, -1, 2)$  correspond to the  $d_{x^2-y^2}$ -wave pairing and  $d_{3z^2-r^2}$ , respectively, both expected to be degenerate under the  $E_g$  representation of the  $O_h$  symmetry group. Notably, numerical results indicate a  $d$ -wave SC characterized by a complex phase structure  $(\Delta_x, \Delta_y, \Delta_z) \propto (1, e^{\pm i2\pi/3}, e^{\pm i4\pi/3})$  is energetically favored in the relevant doping levels.

### D. TRSB $d + id$ Weyl superconductor

The TRSB Weyl SC pairing characterized by  $d_{3z^2-r^2} \pm id_{x^2-y^2}$  is expressed as follows:

$$\begin{aligned} \Delta_\eta(\mathbf{k}) &= \Delta_0 \left( \cos(k_x) + e^{i\eta \frac{2\pi}{3}} \cos(k_y) + e^{i\eta \frac{4\pi}{3}} \cos(k_z) \right) \\ &= \Delta_0 \left( \cos(k_x) - \frac{1}{2} \cos(k_y) - \frac{1}{2} \cos(k_z) \right) + \Delta_0 i\eta \frac{\sqrt{3}}{2} \left( \cos(k_y) - \cos(k_z) \right), \end{aligned}$$

where  $\eta = \pm 1$  corresponds to the two choices of chirality. This pairing belongs to the  $E_g$  irreducible representation of the  $O_h$  point group. The Bogoliubov-de Gennes (BdG) Hamiltonian can be formulated in the two-component Nambu spinor representation as follows:

$$H_{\text{BdG}} = \sum_{\mathbf{k}} \begin{pmatrix} c_{\mathbf{k}\uparrow}^\dagger & c_{-\mathbf{k}\downarrow} \end{pmatrix} H(\mathbf{k}) \begin{pmatrix} c_{\mathbf{k}\uparrow} \\ c_{-\mathbf{k}\downarrow}^\dagger \end{pmatrix}, \quad H(\mathbf{k}) = \begin{pmatrix} \varepsilon(\mathbf{k}) & \Delta(\mathbf{k}) \\ \Delta^*(\mathbf{k}) & -\varepsilon(\mathbf{k}) \end{pmatrix}. \quad (\text{A12})$$

Here, the kinetic energy is given by

$$\varepsilon(\mathbf{k}) = -t \left( \cos(k_x) + \cos(k_y) + \cos(k_z) \right) - \mu$$

where  $t$  represents the effective hopping integral. The Hamiltonian matrix can be expressed in a compact form,

$$H(\mathbf{k}) = \varepsilon(\mathbf{k})\tau_3 + \text{Re}\Delta(\mathbf{k})\tau_1 - \text{Im}\Delta(\mathbf{k})\tau_2 \quad (\text{A13})$$

with  $\tau_i$  ( $i = 1, 2, 3$ ) denoting the Pauli matrices in the Nambu particle-hole space.

The Fermi surface is defined by the condition  $\varepsilon(\mathbf{k}_F) = 0$ , with the eight node points corresponding to:

$$\mathbf{k}_{\text{node}} = \frac{1}{\sqrt{3}}k_F(\pm 1, \pm 1, \pm 1),$$

To investigate these nodes further, we focus on the low-energy effective theory around the two points  $\mathbf{k}_{111} = (1, 1, 1)k_F/\sqrt{3}$  and  $\mathbf{k}_{\bar{1}\bar{1}\bar{1}} = -(1, 1, 1)k_F/\sqrt{3}$ ,

$$\begin{aligned} H_\eta(\mathbf{k}_{111} + \mathbf{p}) &\approx \left( \varepsilon(\mathbf{k}_{111} + \mathbf{p}) - \varepsilon(\mathbf{k}_{111}) \right) \tau_3 + \Delta_0 \sin \frac{k_F}{\sqrt{3}} \left( -p_x + \frac{1}{2}p_y + \frac{1}{2}p_z \right) \tau_1 + \eta \Delta_0 \frac{\sqrt{3}}{2} (-p_y + p_z) \tau_2, \\ H_\eta(\mathbf{k}_{\bar{1}\bar{1}\bar{1}} + \mathbf{p}) &\approx \left( \varepsilon(\mathbf{k}_{\bar{1}\bar{1}\bar{1}} + \mathbf{p}) - \varepsilon(\mathbf{k}_{\bar{1}\bar{1}\bar{1}}) \right) \tau_3 - \Delta_0 \sin \frac{k_F}{\sqrt{3}} \left( -p_x + \frac{1}{2}p_y + \frac{1}{2}p_z \right) \tau_1 - \eta \Delta_0 \frac{\sqrt{3}}{2} (-p_y + p_z) \tau_2 \end{aligned}$$

where the kinetic part near the Fermi surface expands to:

$$\varepsilon(\mathbf{k}_{111} + \mathbf{p}) - \varepsilon(\mathbf{k}_{111}) \approx \tilde{t} \sin \frac{k_F}{\sqrt{3}} (p_x + p_y + p_z), \quad \varepsilon(\mathbf{k}_{\bar{1}\bar{1}\bar{1}} + \mathbf{p}) - \varepsilon(\mathbf{k}_{\bar{1}\bar{1}\bar{1}}) \approx -\tilde{t} \sin \frac{k_F}{\sqrt{3}} (p_x + p_y + p_z)$$

Using an appropriate rescaling of the coordinates, we can write the effective low-energy Hamiltonian as a Weyl form:

$$\begin{aligned} H_\eta(\mathbf{k}_{111} + \mathbf{p}) &\approx + \left[ (\mathbf{v}_1 \cdot \mathbf{p})\tau_1 + \eta(\mathbf{v}_2 \cdot \mathbf{p})\tau_2 + (\mathbf{v}_3 \cdot \mathbf{p})\tau_3 \right], \\ H_\eta(\mathbf{k}_{\bar{1}\bar{1}\bar{1}} + \mathbf{p}) &\approx - \left[ (\mathbf{v}_1 \cdot \mathbf{p})\tau_1 + \eta(\mathbf{v}_2 \cdot \mathbf{p})\tau_2 + (\mathbf{v}_3 \cdot \mathbf{p})\tau_3 \right] \end{aligned} \quad (\text{A14})$$

where the three unit directional vectors are defined as:

$$\mathbf{v}_1 = v\sqrt{\frac{2}{3}} \left( -1, \frac{1}{2}, \frac{1}{2} \right), \quad \mathbf{v}_2 = v\eta\frac{1}{\sqrt{2}} (0, -1, 1) \quad \mathbf{v}_3 = v\frac{1}{\sqrt{3}} (1, 1, 1)$$

and  $v > 0$  is the effective fermi velocity. The magnetic monopole charge in the momentum space associated with these two Weyl points can be calculated as follows:

$$C_\eta(\mathbf{k}_{111}) = \eta \text{Sgn} \left[ \mathbf{v}_1 \cdot (\mathbf{v}_2 \times \mathbf{v}_3) \right] = \eta, \quad C_\eta(\mathbf{k}_{\bar{1}\bar{1}\bar{1}}) = -\eta \text{Sgn} \left[ \mathbf{v}_1 \cdot (\mathbf{v}_2 \times \mathbf{v}_3) \right] = -\eta.$$